Supporting Information

Adhesion, Stiffness and Instability in Atomically Thin MoS_2 Bubbles.

David Lloyd[1], Xinghui Liu[2], Narasimha Boddeti[2], Lauren Cantley[1], Rong Long[2], Martin L. Dunn[3] and J. Scott Bunch[1,4*]

[1]Boston University, Department of Mechanical Engineering, Boston, MA 02215 USA

[2]University of Colorado, Department of Mechanical Engineering, Boulder, CO 80309 USA

[3]Singapore University of Technology and Design, Singapore, 487372

[4]Boston University, Division of Materials Science and Engineering, Brookline, MA 02446 USA

*e-mail: bunch@bu.edu

1. Growth and characterization

Devices were grown by chemical vapor deposition (CVD) according to a method described in an earlier paper[1]. The devices were transferred over the etched microcavities using a PMMA dry transfer method. Immediately prior to transfer the SiO_X wafers were O_2 plasma cleaned for 15 mins to remove any surface contamination. Before annealing off the PMMA layer at 340 ^oC, the devices were left in a vacuum desiccator for > 3 days to allow any gas trapped in the microcavities to leak out. Monolayers were identified by their optical contrast, and their Raman and photoluminescence (PL) spectra (Fig. S1). The separation between the E^1_{2g} and A_{1g} Raman modes was 20.3 cm^{-1}, and the A exciton peak in the PL spectrum was located at 1.88 eV, which demonstrates that the membrane was single layered[2,3]. The E^1_{2g} peak position is later used to determine the residual membrane strain.

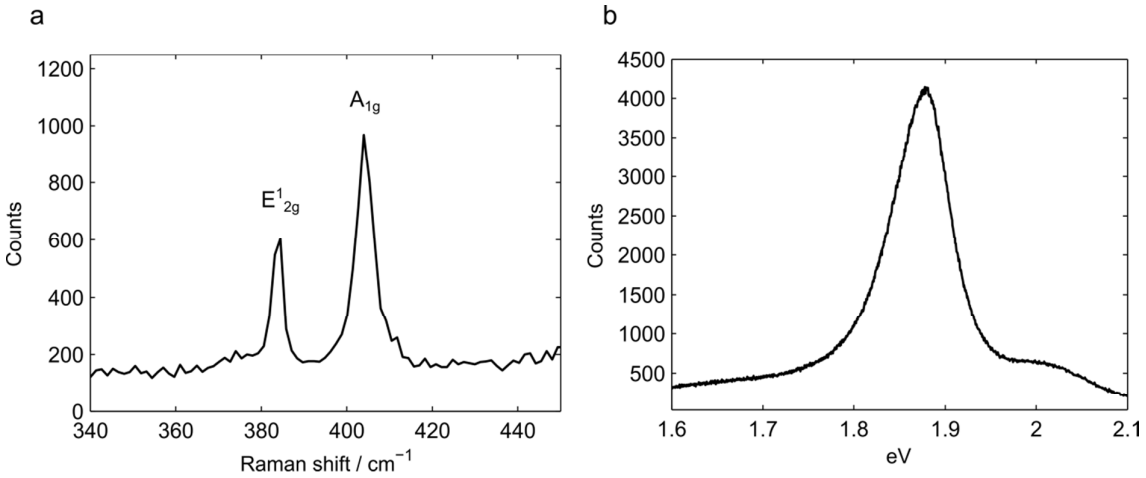

Fig. S1 a) The Raman and b) PL spectrum of a suspended single layer MoS_2 device with zero pressure difference across the membrane.

2. The effect of membrane pre-tension

Even when there is no pressure difference across the membrane there is usually a residual pre-strain observed in suspended devices, due either to the transfer procedure or the membrane sticking to the sidewalls of the cavity[4]. We can estimate the pre-tension in our membranes by using photoluminescence spectroscopy. In an earlier paper[1] we showed that the band-gap in monolayer MoS_2 reduces when biaxial strain is applied, at a rate of -99 meV/%. We took a PL spectrum of a device with no pressure difference across the membrane (Fig. S1), meaning any observed strain would correspond to the pre-strain. We can then convert this to a pre-tension using the formula[5],

$$\sigma_0 = \frac{E_{2D}\varepsilon_0}{1-\nu} \quad \text{(S1)}$$

Our devices have a pre-strain of $\varepsilon_0 < 0.002$ which corresponds to a pre-tension of $\sigma_0 < 0.2$ N/m, which is comparable to previously reported values for atomically thin membranes in this geometry[4,6]. Campbell 1956 [5] showed that when the non-dimensional parameter,

$$P = \frac{\Delta p a E_{2D}{}^{1/2}}{\sigma_0{}^{3/2}} \quad \text{(S2)}$$

satisfies the condition $P > 100$, Hencky's formula in Eq. 1 is correct to within 5%. Most of our data points were taken in a high enough pressure range to satisfy this condition. For instance for the data presented in Fig. 2a, $P = 100$ when $\Delta p = 350$ kPa. Since nearly all of our data was taken with $\Delta p > 350$ kPa we use Eq. 1 to calculate E_{2D}, and neglect the effect of the pre-tension.

3. Work of separation

The full set of data used to produce means and standard deviations of each sample in Fig. 3 of the main text is shown in Fig. S2. Each data point represents the measured value of Γ_{sep} for an individual device of a given sample.

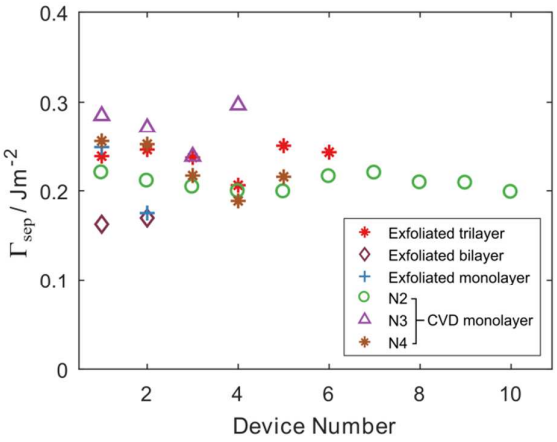

Fig. S2. All Γ_{sep} data used to calculate means and standard deviations of each sample in Fig. 3.

4. Free energy model including adhesion hysteresis

We can interpret the results described in Fig. 4 of the main text using the free energy model described in Eq. 1. Taking the derivative of F with respect to a, and substituting the pressure terms for the Hencky's result in Eq. 3 yields,

$$\frac{dF}{da} = 2\pi a\left[\Gamma - \frac{5}{4}CKE_{2D}\left(\frac{\delta}{a}\right)^4\right] \quad \text{(S3)}$$

Setting this formula equal to zero to find the radius at which the free energy is minimized leads to,

$$\Gamma_{sep} = \frac{5}{4}CKE_{2D}\left(\frac{\delta}{a}\right)^4 \quad \text{(S4)}$$

The constants C and K depend only on the Poisson's ratio v, and their values for various 2D materials are tabulated in Table S1.

	Poisson's Ratio *v*	*K(v)*	*C(v)*
MoS_2	0.29	3.54	0.522
Graphene	0.16	3.09	0.524
hBN	0.22	3.28	0.523
Black Phosphorus	0.4	4.07	0.519

Table S1. Values for constants *C(v)* and *K(v)* for several 2D crystals, calculated using Hencky's solution.

We plot the relationship described by Eq. S4 in Fig. S4a with a value of $\Gamma_{sep} \sim 220$ mJ/m^2 and find our data fits this relationship very well. This formula is independent of whether N is increasing or decreasing, so when our devices are left to deflate we should expect δ and a to return along the same path as during inflation, and described by Eq. S4.

We can explain the difference between inflation and deflation we see in our data as a result of *adhesion hysteresis*, whereby the energy required to separate the membrane from the surface Γ_{sep} is greater than the energy returned to the system as the membrane re-adheres Γ_{adh}, with $\Gamma_{adh} < \Gamma_{sep}$.

For changes of the device radius Δa, we now have:

$$\Gamma = \begin{cases} \Gamma_{adh}, & \Delta a < 0 \\ \Gamma_{sep}, & \Delta a > 0 \end{cases} \quad \text{(S5)}$$

As the device inflates and $\Delta a > 0$, the free energy of the system is minimized according to Eqs. 4 and 5, with $\delta_0/a_p \sim \Gamma_{sep}^{1/4}$. When deflating the radius of the device will only decrease when $dF/da > 0$ for $\Delta a < 0$ (with $\Gamma=\Gamma_{adh}$), in order for the free energy to be minimized. From examining Eq. S3 and considering that $\Gamma_{adh} < \Gamma_{sep}$, this will only occur when δ has decreased from δ_0 to below the critical value of $\delta = \delta_c$ after which the device radius can reduce in the form of a snap-in transition. Since the radius cannot decrease until δ_c is reached, the bubble edge remains pinned at a_p. The critical deflection δ_c marks the point where $dF/da = 0$ for $\Delta a < 0$ (i.e. $\Gamma=\Gamma_{adh}$), and from using Eq. S3 we can see that this occurs when the relationship,

$$\Gamma_{adh} = \frac{5}{4} C K E_{2D} \left(\frac{\delta_c}{a_p}\right)^4 \quad \text{(S6)}$$

is satisfied. This corroborates with what we see in Fig S3a, in which the value of δ_c is roughly proportional to a_p for the devices measured. We can estimate the value of Γ_{adh} by fitting this relationship to the values of δ_c and a_p of devices just before the snap in transition occurs, and we plot this line of best fit in Fig. S3a which corresponds to $\Gamma_{adh} \sim 14$ mJ/m^2. We checked the repeatability of our measurements of Γ_{adh} by repeating the experiment 6 times on a single device, which resulted in a mean and standard deviation of 13 mJ/m^2 and 5 mJ/m^2 respectively (Fig. S3b).

These arguments are best seen graphically in terms of the free energy landscape plotted as a function of radius in Fig S4b, c and d. In the absence of adhesion hysteresis, as the pressure inside the device decreases and the devices deflate, the free energy minima moves to a smaller radius (Fig. S4b). The path taken by our devices is shown in Fig. S4c, and clearly shows the devices not following the local minima in the free energy. By introducing adhesion hysteresis into the model (Fig. S4d), ΔF is calculated using Γ_{sep} for $\Delta a > 0$ and Γ_{adh} for $\Delta a < 0$, which results in the device radius remaining trapped in a local minima as the device deflates. The radius only changes when $dF/da > 0$ for $\Delta a < 0$ which only happens when Eq. S6 (Eq. 5 in the main text) is satisfied.

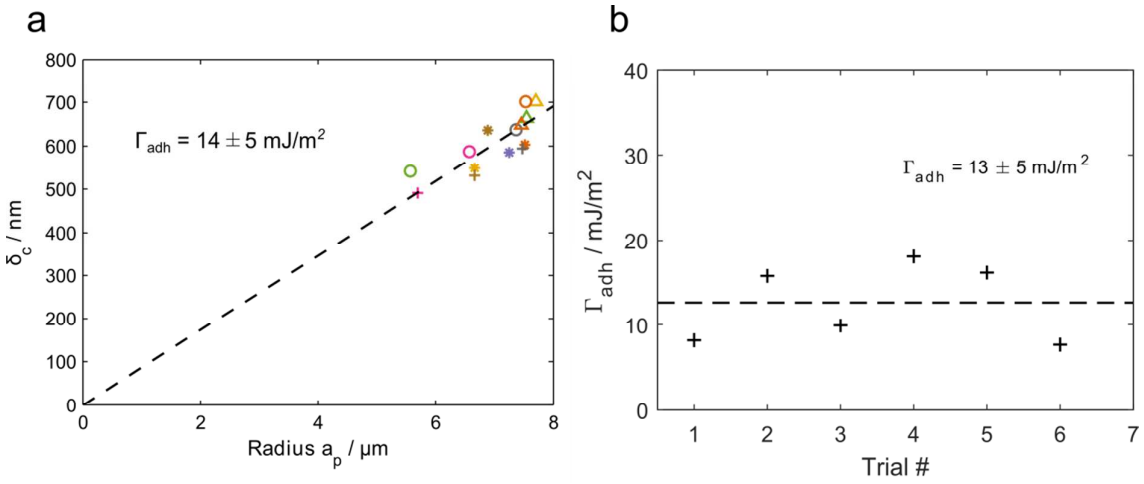

Fig. S3 a) Data for devices measured on sample *N2*, showing the values of δ_c and a_p just before snap-in used to calculate Γ_{adh}. Each color/symbol represents a different device. b) Multiple measurements of a single device at a number of different pressures showing repeatability. Dashed line represents the mean adhesion value.

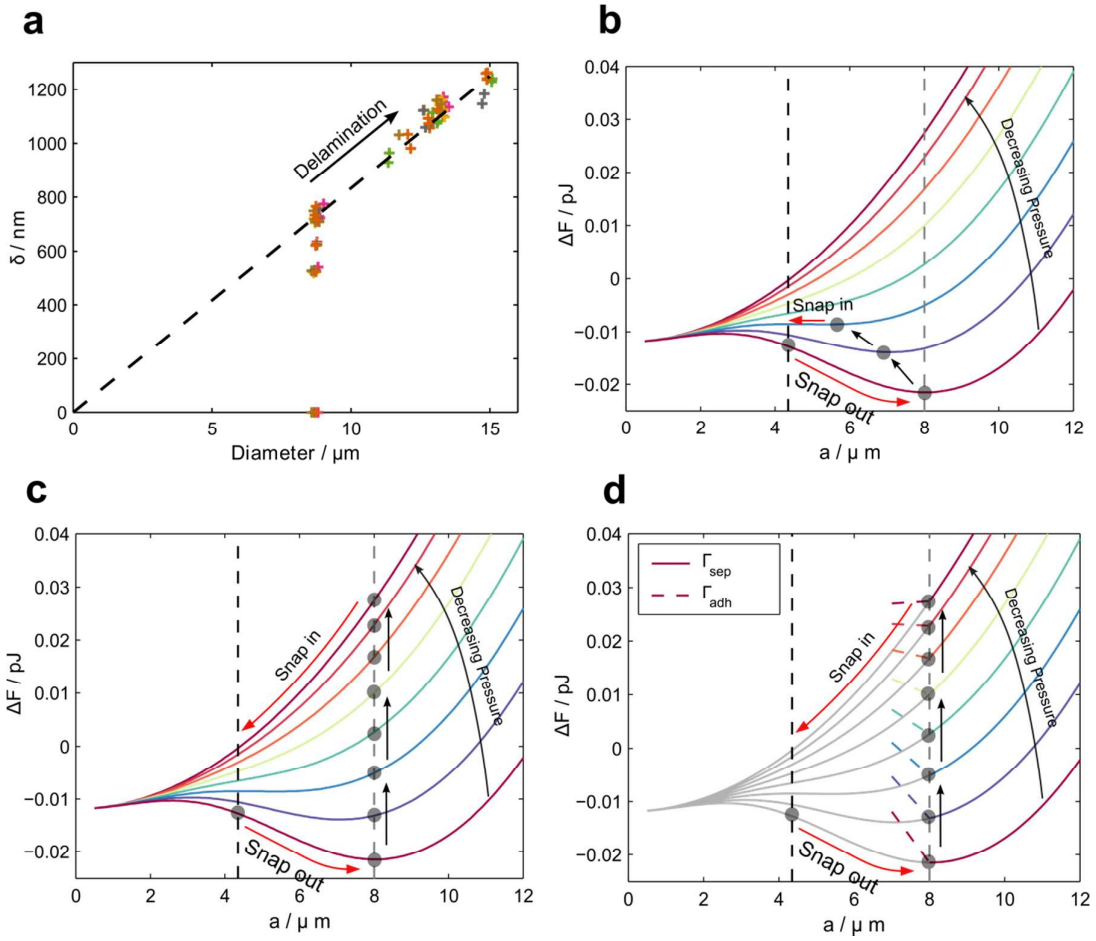

Fig. S4 a) As devices delaminate the ratio δ/a remains constant according to Eq. S4. b) The free energy landscape if there is no adhesion hysteresis. The device radius is that which minimizes the free energy, and the grey dots mark the path we would expect the device to take. c) The actual path our

devices take, which appears to not minimize the free energy. d) The modified free energy landscape if $\Gamma_{adh} < \Gamma_{sep}$. As the device reduces its radius its free energy is determined by the dashed lines. The device is now trapped in a free energy minima and snap-in only occurs when the gradient of the dashed line is greater than zero.

To see if the work of adhesion varied between samples fabricated with the same method of CVD growth and transfer, we performed measurements of 5 different CVD samples (*N2-6*) with at least 4 devices measured per sample. Monolayer devices were delaminated and left to deflate, and AFM measurements of δ_c and a_p taken just before snap-in were used to calculate the work of adhesion using Eq. S6. The data is presented in Fig. S5a, with each data point representing a measurement of Γ_{adh} in a single device of a given sample. The mean and standard deviations of each sample are shown in Fig. S5b. Between different samples there is considerable variation in the mean work of adhesion, which suggests that factors such as the cleanliness of substrate or membrane which can vary from sample to sample may play significant roles in adhesion hysteresis. A few of the devices measured did not snap in completely from radius a_p to a_0, but rather initially snapped in to an intermediate radius followed by a second snap in to a_0 (Fig. S9b). All the transitions between these states were unstable and occurred in less than one second.

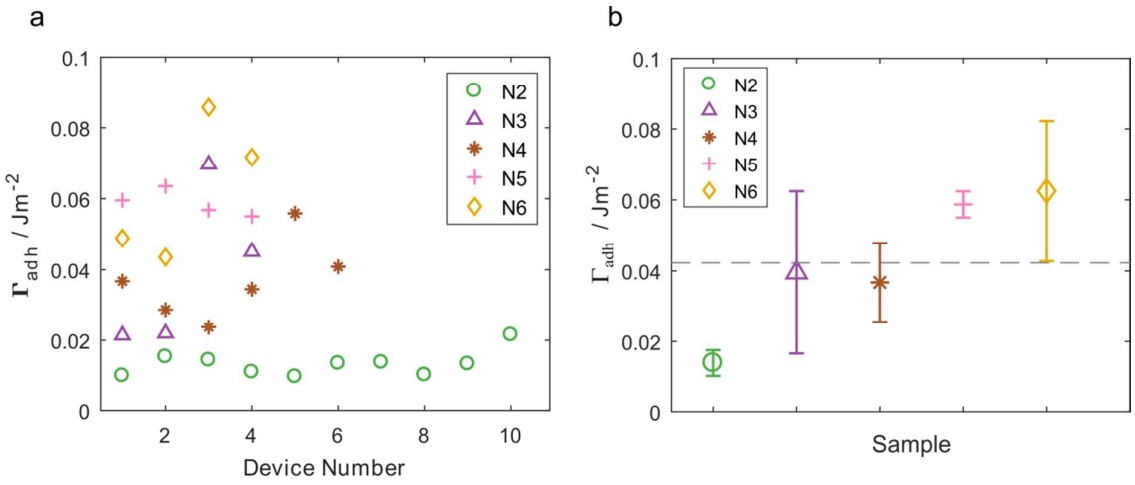

Fig. S5 a) Work of adhesion for every device measured in each sample. b) Mean and standard deviations of the work of adhesion in each sample. The dashed line represents the mean of the 5 samples.

5. Contact angle of bubbles during deflation

Instead of analyzing the snap-out and snap-in data in terms of δ and a, an analogous method is to measure the contact angle θ_c between the membrane and the substrate (see Fig. S6 inset) using an AFM. In Fig. S6 we plotted the contact angle against the radius of a device as it is inflated (black) and then left to deflate (red). As the device is inflated the contact angle increases until a critical value, at which point the device delaminates with the contact angle remaining constant. When the device is left to deflate the contact angle decreases at constant radius until another critical contact angle is reached, at which point the device undergoes the snap-in transition.

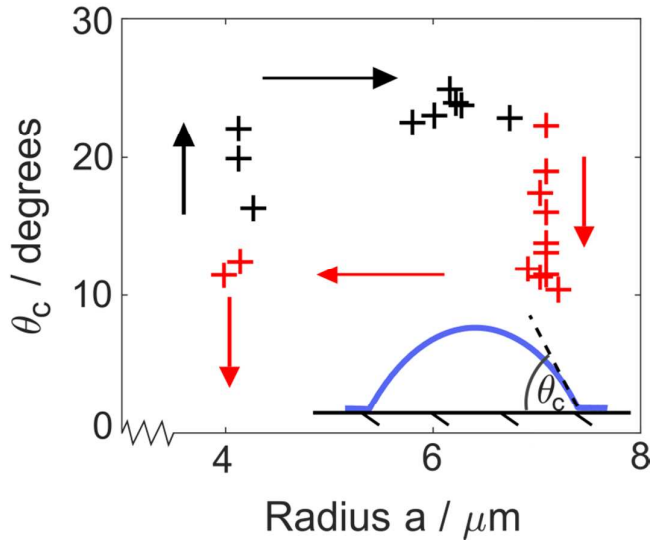

Fig. S6. The contact angle of a device during inflation (black) and deflation (red).

6. Strain trapping around the edge of the membrane

To investigate a possible mechanism for the observed adhesion hysteresis we used Raman spectroscopy to measure the strain distribution around our devices. The peak positions of the Raman modes in monolayer MoS_2 are known to be sensitive to strain[1,7], so by measuring how these peaks shift at different locations around the device we can build up an image of how strain is distributed. For these measurements we used the E^1_{2g} peak to estimate the strain (Fig. S1), since it has a peak position which is strain sensitive and independent of doping effects.

Fig. S7a shows an AFM image of a device delaminated to $a_p \sim 7.5$ μm, which was then left to deflate and undergo the snap-in transition. A Raman map was then taken after snap-in (Fig S7b), with the strain calculated from the position of the E^1_{2g} peak using the reported shift rate of ~ 5 cm^{-1} / %[1,7]. A region of $\varepsilon \sim 0.5\%$ can be clearly seen around the circumference of where the delaminated bubble was before snap-in. This strain likely originates from the pressure induced radial strain at the edge of the bubble, which for these devices is ~1.5% (Fig. S8d). Using this upper bound of $\varepsilon \sim 1.5\%$ and the formula for the isotropic strain membrane energy density[8], $U = \frac{1}{2} E_{2D} \varepsilon^2$, we can estimate the energy stored in the strained regions to be $U \sim 20$ mJ / m^2, which can account for some but not all the energy dissipation which produces a difference between Γ_{adh} and Γ_{sep}. The presence of strain in the membrane also implies some contribution of energy dissipation through friction as the membrane changes its length on the surface of the substrate[9].

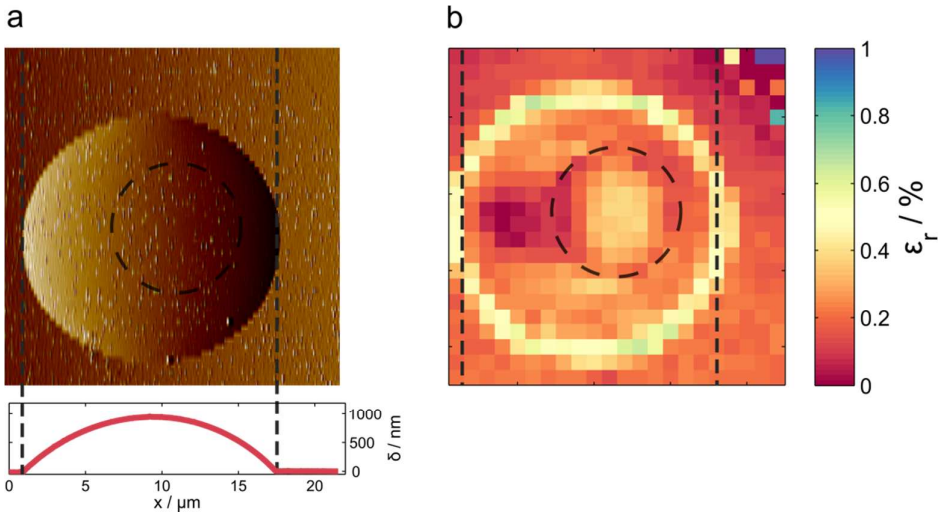

Fig. S7 a) AFM image (amplitude channel) of a delaminated device before the snap-in transition. The position of the microcavity is marked by a dashed circle. Below is a cross section of the device. b) Strain map of the same device after the snap-in transition when the device has fully deflated. Strain is calculated using the peak shift in the E^1_{2g} Raman mode at each point. Each pixel is 1 x 1 μm and corresponds to a single Raman scan.

In order to observe the process by which this strain becomes 'trapped' in the membrane around the device, we took Raman line scans over a cross section of a device as it deflated and plotted the E^1_{2g} peak position as a function of distance (Fig. S8a and S8b). Before each Raman scan we found the corresponding geometry of the device by taking an AFM image (Fig. S8c). Across the delaminated bubble region (marked by dashed lines) the peak shift abruptly increases at the edge of the bubble, followed by a gradual increase towards the center of the device. In Fig. S8d we used Hencky's solution to find the predicted strain profile across the device for its initial geometry (Fig. S8c red line) before deflation. In the model, the

strain jumps from zero to purely radial tensile strain at the edge of the device, with the tangential component gradually increasing from zero to be equal to the radial component at the center. The E^1_{2g} peak position depends on contributions of both the radial and tangential strain, so this model explains the profile seen in Fig. S8a.

Fig. S8b shows that a region of strain extends ~1.5 μm outside the edge of the bubble in the initial Raman scan (red line). As the device deflates and the radius remains pinned the peak shift across the delaminated region of the membrane reduces as it becomes less strained, however the region of strain outside bubble remains roughly constant throughout deflation. These results show that the ring of strain in Fig. S7b is formed when the device initially delaminates, and that this strain does not relax as the device deflates and eventually snaps in.

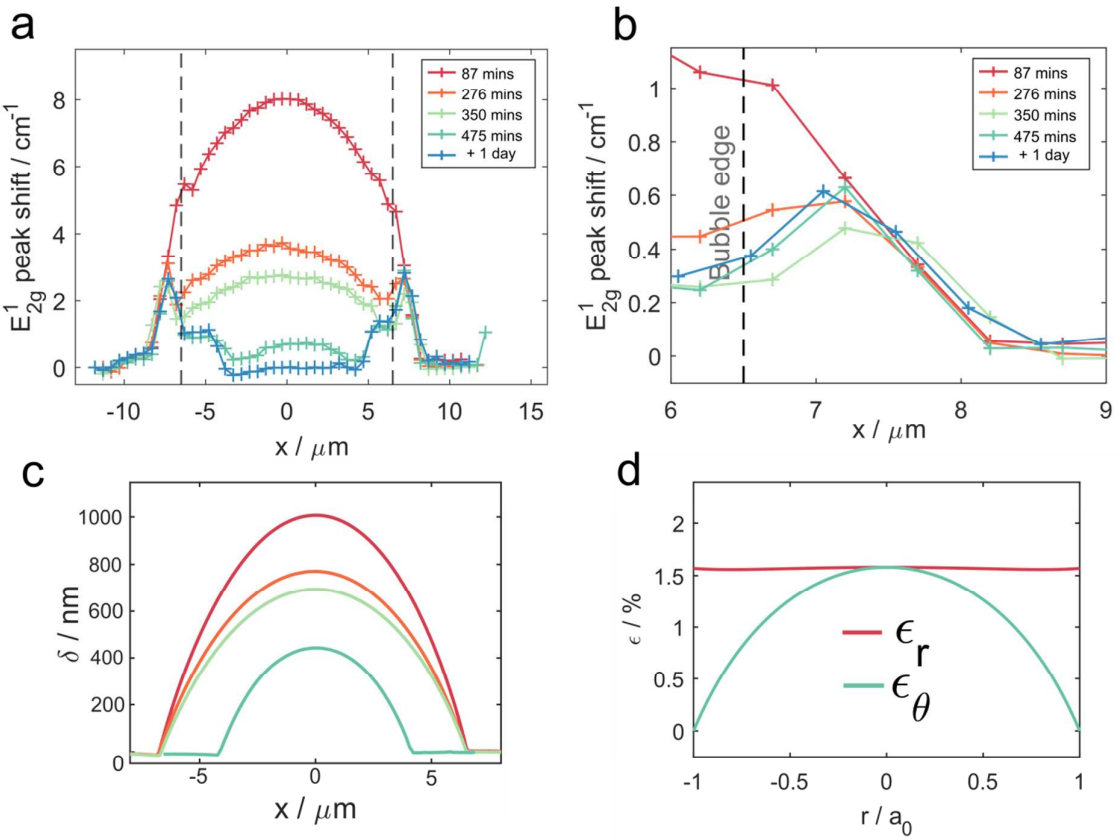

Fig. S8 a) Raman line scans over a device over time as it deflates. Dashed vertical lines mark the edge of the delaminated bubble. b) A zoomed in version of a) focusing on the edge region of the device. c) AFM cross sections of the device at each time, using the same color scheme as in a). d) Radial (ε_r) and tangential (ε_θ) components of the strain as a function of radius for this device's initial geometry before deflating, calculated using Hencky's model with values for δ and a taken from the red curve in c).

7. The effect of the slipping of the membrane on E_{2D} calculations

The strain at the edge of the bubble introduces extra slack into the membrane of bubble, which may affect our measurements of E_{2D}. We can estimate the effect this has on our measurements by integrating the strain over the strained region at the edge of the bubble in Fig. S8b to find the total extra slack, ΔL, added to the bubble membrane. We can write the slack added to the membrane as,

$$\Delta L = \int_0^{x_1} \varepsilon(x) dx \tag{S7}$$

The initial measurement in Fig. S8b (red line color and labeled '87 mins') shows that the peak shift linearly decreases from ~ 5.5 cm^{-1} around the edge of the device to ~0 cm^{-1} at 1.5 μm outside the device radius, so we take x_1 = 1.5 μm. To find $\varepsilon(x)$ we take ε ~ 1.5 % at the edge of the device (Fig. S8d) and use the linear strain profile seen in Fig. S8b, which leads to $\varepsilon(x) \sim (0.015/1.5)\, x$ μm^{-1}. This gives ΔL ~ 11 nm over a device radius of 6.5 μm. This reduces the pre-strain by ~ 0.0017 which is about the same as the initial pre-strain. We therefore take this change to be negligible in to the pressure range we are studying due to the arguments made in section 2.

8. Stable delamination devices

Devices of well depth d ~ 650 nm were fabricated that exhibited stable delamination (Fig. S9). These devices showed the same hysteric behavior as our other devices. To calculate the work of separation of these devices we used Eq. 4 in the main text with AFM measurements of δ and a, and used the mean E_{2D} of all our CVD devices of 128 N/m. We measured 3 devices over 4 different pressures, and found a value of Γ_{sep} = 207 ± 19 mJ/m^2. We also measured the work of adhesion of the device shown in Fig. S9b, which we found to be Γ_{adh} = 40 mJ/m^2.

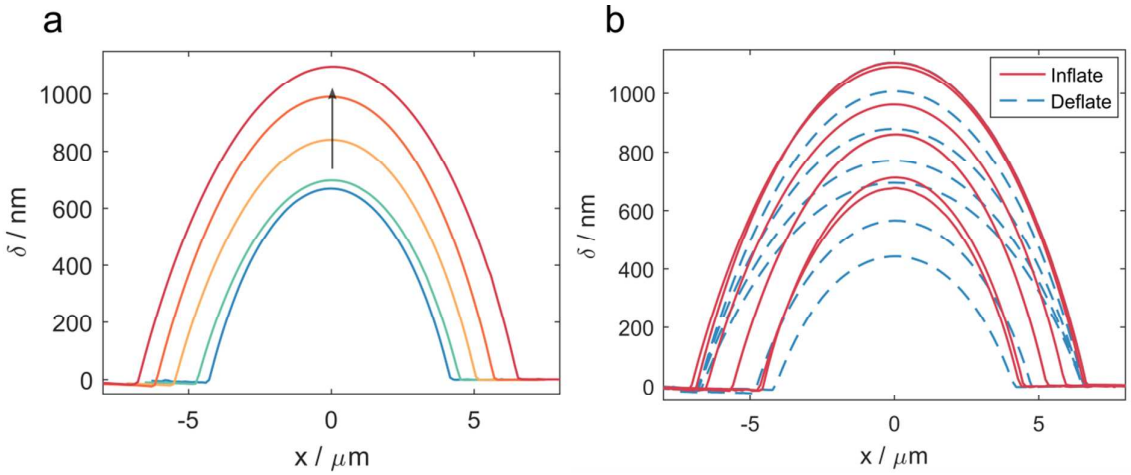

Fig. S9 a) Stable delamination with increasing pressure. b) A device which delaminates stably with increasing pressure, but shows adhesion hysteresis upon deflation. This device snapped in to an intermediate step before fully re-laminating to the substrate.

9. Additional snap-in data

Fig. S10 shows the complete data set for our snap-in measurements presented in Fig. 4b of the main text. This data was taken using an AFM in tapping mode. To confirm that the forces from to the AFM tip were not affecting our results, we measured the snap-in of a device as it deflated by using solely optical measurements. We took sequential PL spectra at the center of the device as it deflated, where the membrane is under biaxial strain. In an earlier paper[1] we found that the PL peak red-shifts under biaxial strain by -99 meV/%, so PL measurements allow us to measure the biaxial strain ε in the device. We can also measure the radius a of the device as it deflates using an optical microscope. Using these values for a and ε we can estimate the deflection of the device using the formula,

$$\varepsilon = \sigma(\nu)\left(\frac{\delta}{a}\right)^2 \tag{S8}$$

where $\sigma(\nu)$ is a numerical constant which depends only on Poisson's ratio ν , and in this case $\sigma = 0.709$. We measured a deflating device using the non-contact optical method, after which we re-inflated the device to the same pressure and used the AFM to measure the geometry of the device as it deflated. We compare the results of these two methods in Fig. S10b, and find very similar results in the two cases. The device appears to snap-in at a slightly lower δ in the AFM measurements, however this is likely due to the long scan times (~3 min) required to take a PL spectrum meaning that we couldn't measure the device right at the moment before snap-in.

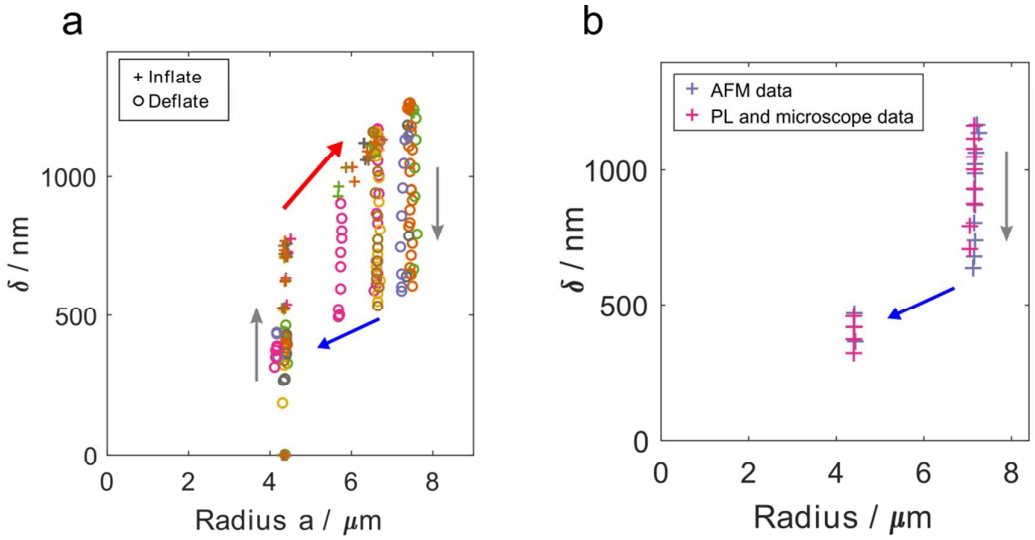

Fig. S10 a) Complete data containing all data points of results presented in Fig. 4b in the main text. Each color represents a different device. b) Comparison of snap-in transitions measured optically or by AFM. For optical measurements a is determined using an optical microscope with a 100x objective, and δ is determined from the PL peak position and Eq. S8.

10. Young's modulus

Fig. S11 shows the complete data set used to calculate the Young's modulus for each device in Fig. 2b in the main text.

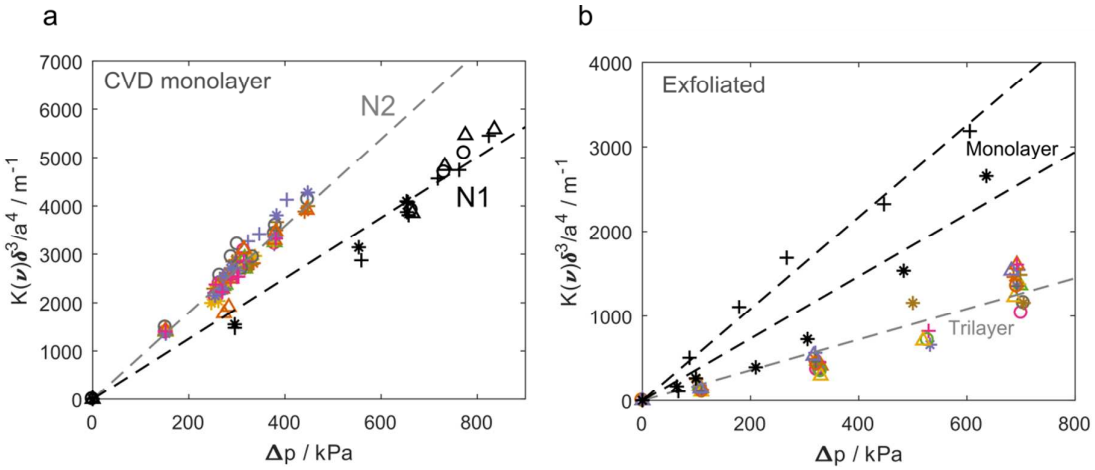

Fig. S11 a) CVD monolayer devices from sample *N1* and *N2*. b) Exfoliated monolayer and trilayers devices. Dashed lines are plotted for each of the sample means reported in Fig. 2c of the main text. Different color/symbols represent different devices.

11. Videos of snap transitions

Video 1 shows the snap-in transition of a deflating device taken with a high speed camera. The snap-in transition occurs faster than the frame rate of the camera (0.5 ms). Video 2 shows a device in a pressure chamber with a quartz window, allowing us to observe a delaminated device as the chamber pressure is increased and decreased (video speed is 4x). For the first half of the video the external pressure is increased, with the delaminated device snapping-in at ~6 s. During the second half of the video the pressure is decreased, with the device snapping-out at ~30 s.

References

(1) Lloyd, D.; Liu, X.; Christopher, J. W.; Cantley, L.; Wadehra, A.; Kim, B. L.; Goldberg, B. B.; Swan, A. K.; Bunch, J. S. *Nano Lett.* **2016**, *16*, 5836−5841.

(2) Lee, C.; Yan, H.; Brus, L. E.; Heinz, T. F.; Hone, J.; Ryu, S. *ACS Nano* **2010**, *4* (5), 2695–2700.

(3) Mak, K. F.; Lee, C.; Hone, J.; Shan, J.; Heinz, T. F. *Phys. Rev. Lett.* **2010**, *105* (13), 2–5.

(4) Bunch, J. S.; Verbridge, S. S.; Alden, J. S.; Van Der Zande, A. M.; Parpia, J. M.; Craighead, H. G.; McEuen, P. L. *Nano Lett.* **2008**, *8* (8), 2458–2462.

(5) Campbell, J. D. *Quart. Journ. Mech. Appl. Math* **1956**, *IX*, 84–93.

(6) Wang, L.; Travis, J. J.; Cavanagh, A. S.; Liu, X.; Koenig, S. P.; Huang, P. Y.; George, S. M.; Bunch, J. S. *Nano Lett.* **2012**, *12*, 3706–3710.

(7) Conley, H. J.; Wang, B.; Ziegler, J. I.; Haglund, R. F.; Pantelides, S. T.; Bolotin, K. I. *Nano Lett.* **2013**, *13* (8), 3626–3630.

(8) Gould, P. L. *Introduction to Linear Elasticity 3rd ed.*; 2013.

(9) Kitt, A. L.; Qi, Z.; Remi, S.; Park, H. S.; Swan, A. K.; Goldberg, B. B. *Nano Lett.* **2013**, *13*, 2605−2610.